JPE 17-6-21

https://doi.org/10.6113/JPE.2017.17.6.1611
ISSN(Print): 1598-2092 / ISSN(Online): 2093-4718

# Research and Stability Analysis of Active-Disturbance-Rejection-Control-Based Microgrid Controllers

Xiaoning Xu[†,**], Xuesong Zhou[*,**], Youjie Ma[**], and Yiqi Liu[***]

[†,*]School of Electrical and Information Engineering, Tianjin University, Tianjin, China
[**]School of Electrical and Electronic Engineering, Tianjin University of Technology, Tianjin, China
[***]College of Mechanical and Electrical Engineering, Northeast Forestry University, Harbin, China

## Abstract

With the rapid development of microgrid technology, microgrid projects are no longer limited to laboratory demonstrations and pilot platforms. It shows greater value in practical applications. Hence, the smooth interaction between a microgrid and the main grid plays a critical role. In this paper, a control method based on active disturbance rejection control (ADRC) is proposed in order to realize seamless transitions between grid-connected and islanding operation modes and stable operation with variable loads. It is verified by simulations that the proposed ADRC-based method features better performance when compared to conventional proportional-integral-differential (PID) control. Meanwhile, the stability of the third-order extended state observer (ESO) in second-order ADRC is validated by using Lyapunov stability criteria.

**Key words:** Active disturbance rejection control, Lyapunov stability criteria, Microgrid, Third-order extended state observer

## I. INTRODUCTION

Nowadays, with the limited amount of fossil fuel and increasing environmental concerns, traditional power systems all over the world have been significantly changed with energy management methods migrating from centralized generation to distributed generation. Plenty of technical research has been conducted in the European Union (EU) under the 5th, 6th and 7th framework program with the goal of sustainable energy and distributed generation [1]. A microgrid is comprised of various types of distributed sources as well as energy storage, load and control units to form an isolated power system. Meanwhile, microgrids can be connected to the main grid [2]. With its operational flexibility, the power availability of critical loads can be uninterrupted. Many countries, such as those in the EU, the United States of America, Canada, Japan, etc., have been involved in microgrid research by means of laboratory demonstrations and pilot projects. Most of the work has been done in regards to microgrid operation, protection, control, energy management and the impact of microgrids on conventional power systems.

The operation modes of microgrids can be classified into three categories, i.e., grid-connected mode, islanding mode and the transition process between them. Microgrid related research is no longer only focused on islanding operation. Coordination between different operation modes is a prerequisite for the smooth interaction between a microgrid and the main grid.

Since renewable energy sources are dispersedly connected to the common bus in a microgrid, the control and operation of power electronic interface inverters is a key issue in the operation of microgrids [10], [11].

Droop control is widely employed as a decentralized method for load power sharing. Output current sharing accuracy is degraded due to the effect of a voltage drop across the line impedance. This effect is similar to the reactive power sharing in a microgrid. To enhance the reactive power sharing accuracy in a microgrid, several methods for improved droop control have been proposed [9]. A compensating method was put forward in which the remote voltage signal is measured and an

Manuscript received Jan. 13, 2016; accepted Jul. 6, 2017
Recommended for publication by Associate Editor Kyeon Hur.
[†]Corresponding Author:xxn2523@126.com
Tel: +86-136-1208-2683, Tianjin University of Technology
[*]School of Electrical and Information Eng., Tianjin University, China
[**]School of Electrical and Electronic Eng., Tianjin Univ. of Tech., China
[***]College of Mechanical and Electrical Eng., Northeast Forestry University, China

integrator term in the conventional Q-V droop control is employed [12]. The voltage amplitude in the Q-V droop control was replaced by a variable representing the time rate of the change in the voltage magnitude [13]. The voltage droop across the impedance was estimated in grid-connected operation to reach the modified slope in the Q-V droop control [14]. A modified control based on the conventional droop control is implemented based on feed-forward current control, which allows the converter to work in several modes and permits the inverter to work as a grid supporting source or as an ancillary service provider when it works in the grid-connected mode [15]. In [16], decoupled droop control techniques were proposed and analyzed to obtain the independent relationship between the frequency vs. active power and the voltage vs. reactive power. The maximum load flow is also an important factor in the conventional droop control [9]. In [17], it is proposed that the maximum load flow is considered in droop-control-associated optimal power flow problems.

Furthermore, the integration of single-phase loads in microgrids can also induce unbalanced voltage and current in islanding operation. A control algorithm in the time domain can cope with this issue and stabilize the output of the grid-connected controller by detecting the negative sequence voltage and current [18]. In [19] and [20], the impact of unbalanced and non-linear loads on different microgrid operation modes are further analyzed. Meanwhile, the detection and elimination of unbalance currents have been proposed.

In order to achieve smooth transitions between the grid-connected and islanding modes, proportional-integral-differential (PID) control and some other modern control algorithms are commonly employed [9]–[20]. However, PID control has inherent drawbacks and modern control algorithms are to some extent impractical in power electronic inverter control [24].

Active disturbance rejection control (ADRC) is proposed based on consideration of the existing drawbacks of modern control theory and the advantages of conventional PID control. It does not depend on an accurate mathematic model and it utilizes an extended state observer (ESO) to detect and compensate the disturbance in a system. So far, the ADRC method has been applied in aviation, precise instrumentation, generator control and some other applications.

To realize the stable operation of microgrids, the advanced ADRC method is applied in this paper to design a microgrid controller. Based on a microgrid with two distributed generators (DGs), a second-order ADRC controller is implemented. It is used to control and output voltage and current in the d and q axis simultaneously. Meanwhile, the coupled terms are regarded as disturbances to be eliminated. Hence, seamless transitions between grid-connected and islanding modes can be achieved. A microgrid simulation platform with two DGs is implemented in MATLAB/Simulink. Both PID and ADRC based methods are tested and compared. It can be demonstrated that based on the detection and compensation of inside and outside disturbances by using a third-order ESO, the ADRC method can ensure flexible interactions between microgrids and the main grid during operation mode transitions and load variations.

Moreover, Lyapunov stability theory is used to verify the stability of a third-order ESO in a second-order ADRC.

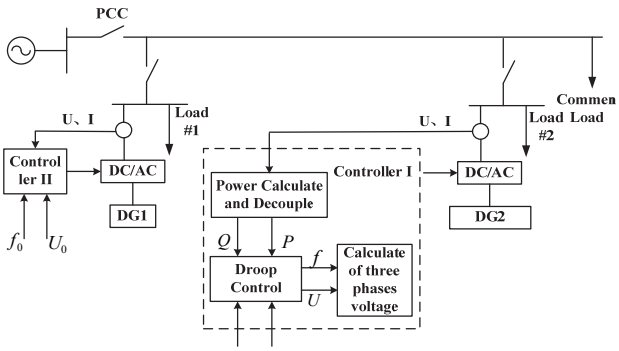


Fig. 1. Typical configuration of a microgrid.

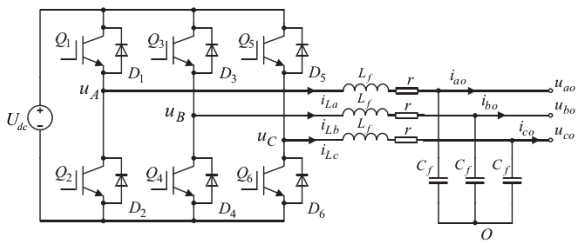


Fig. 2. Three-phase voltage source inverter in a microgrid.

## II. Typical Microgrid Configuration and Inverter Model

### *A. Typical Microgrid Configuration*

The typical configuration of a microgrid is shown in Fig. 1. A microgrid is commonly comprised of multiple DGs. As an example, two DGs are included in this system. Meanwhile, the DC side of each DG is considered as a constant DC source. PMW inverters are used for DC sources to generate three-phase signals at the AC side. LC filters are used to eliminate high-order harmonics, while power cables, switches and transformers are used to interconnect the local DGs to the main grid. In terms of the two DGs, droop control is used for DG #1, and the frequency and voltage are established by using DG #1. Meanwhile, DG #2 runs in the PQ operation mode and supports the active and reactive power to the grid. It can be seen that the most common approach for connecting DGs to the main grid is to use a voltage source interface inverter [21], [22]. Hence, the operation of the DG units is essentially implemented based on the control of the interface inverters.

### *B. Typical Configuration of the Interface Inverter and its Mathematical Model*

The typical configuration of a voltage source interface inverter in a microgrid is shown in Fig. 2.

In Fig. 2, $u_{dc}$ represents the DC source voltage, $L_f$ represents the filter inductance, $r$ represents the equivalent filter resistance, $C_f$ represents the filter capacitor. Meanwhile, $u_A$, $u_B$ and $u_C$ represent the middle point voltages of each phase, $O$ is the neutral point of the filter capacitor, $u_{ao}$, $u_{bo}$ and $u_{co}$ are the capacitor voltages, $i_{La}$, $i_{Lb}$ and $i_{Lc}$ are the inductor currents, and $i_{ao}$, $i_{bo}$ and $i_{co}$ are the inverter output currents.

By using the Kirchhoff voltage and current theory, it can be derived that:

$$\begin{cases} u_A - u_{ao} = L_f \dfrac{di_{La}}{dt} + r i_{La} \\ u_B - u_{bo} = L_f \dfrac{di_{Lb}}{dt} + r i_{Lb} \\ u_C - u_{co} = L_f \dfrac{di_{Lc}}{dt} + r i_{Lc} \\ i_{La} - i_{ao} = C_f \dfrac{du_{ao}}{dt} \\ i_{Lb} - i_{bo} = C_f \dfrac{du_{bo}}{dt} \\ i_{Lc} - i_{co} = C_f \dfrac{du_{co}}{dt} \end{cases} \tag{1}$$

By collecting (1), a mathematical model in the d-q axis can be obtained:

$$\frac{d}{dt}\begin{bmatrix} u_{od} \\ u_{oq} \\ i_{Ld} \\ i_{Lq} \end{bmatrix} = \begin{bmatrix} 0 & \omega & \dfrac{1}{C_f} & 0 \\ -\omega & 0 & 0 & \dfrac{1}{C_f} \\ -\dfrac{1}{L_f} & 0 & -\dfrac{r}{L_f} & \omega \\ 0 & -\dfrac{1}{L_f} & -\omega & -\dfrac{r}{L_f} \end{bmatrix} \begin{bmatrix} u_{od} \\ u_{oq} \\ i_{Ld} \\ i_{Lq} \end{bmatrix} + \begin{bmatrix} -\dfrac{1}{C_f} i_{od} \\ -\dfrac{1}{C_f} i_{oq} \\ \dfrac{u_d}{L_f} \\ \dfrac{u_q}{L_f} \end{bmatrix} \tag{2}$$

Assuming that the three-phase voltage is represented as:

$$\begin{cases} u_a = U_m \cos(\omega t) \\ u_b = U_m \cos(\omega t - 2\pi/3) \\ u_c = U_m \cos(\omega t + 2\pi/3) \end{cases} \tag{3}$$

where *Um* is the amplitude of the three-phase voltage. By using Park's transformation, it yields that:

$$\begin{cases} u_d = U_m \\ u_q = 0 \end{cases} \tag{4}$$

By using the instantaneous active and reactive power theory, the power exchange between a local microgrid and the main grid is reached as:

$$\begin{cases} P(t) = u_d(t) i_d(t) + u_q(t) i_q(t) \\ Q(t) = u_q(t) i_d(t) - u_d(t) i_q(t) \end{cases} \tag{5}$$

It can be seen that by adjusting the grid-connected current in the d-q axis, the power exchange between the microgrid and the main grid can be regulated.

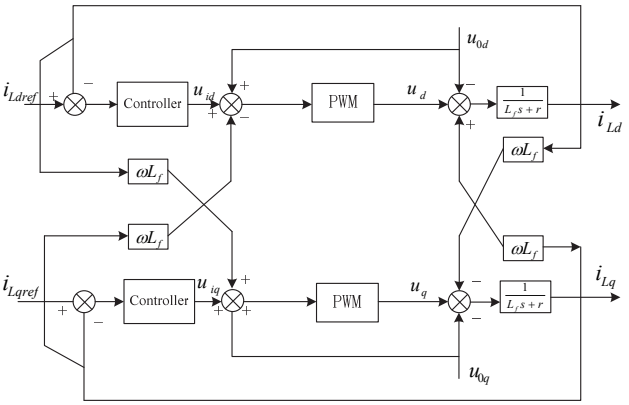


Fig. 3. Coupling terms between $i_d$ and $i_q$.

Based on the results in (2), its differential expression can be shown as:

$$\begin{cases} L_f \dfrac{di_{Ld}}{dt} = u_d - u_{od} + \omega L_f i_{Lq} - r i_{Ld} \\ L_f \dfrac{di_{Lq}}{dt} = u_q - u_{oq} - \omega L_f i_{Ld} - r i_{Lq} \end{cases} \tag{7}$$

It can be seen that $i_d$ and $i_q$ are highly coupled, and that they influence each other. This phenomenon can also be shown in the control diagram in Fig. 3.

The coupling term between $i_d$ and $i_q$ impacts the current control effect. If this coupling is not properly eliminated, the performance of the microgrid controller is degraded, and the difficulty of obtaining a smooth operation mode transition is increased.

Since ADRC does not rely on a model and is free of parameter derivations, it can be applied to coupled current control. These coupling terms can be included in system disturbances. By using ESO, they can be easily estimated and compensated.

## III. Design of a Second Order ADRC Controller

### *A. Active Disturbance Rejection Control*

ADRC is derived based on the conventional feedback theory in PID control by Dr. Jingqing Han. Its basic idea is to use an extended state observer to estimate and compensate overall system disturbances, including both external and internal disturbances. Hence, a control diagram that is free from disturbance is established [26], [27]. A control diagram of ADRC is shown in Fig. 4.

It can be seen that an ADRC system is commonly comprised of three parts, i.e., a tracking differentiator (TD), an extended state observer (ESO) and a nonlinear state error feedback (NLSEF).

### *B. Design of the Microgrid Controller*

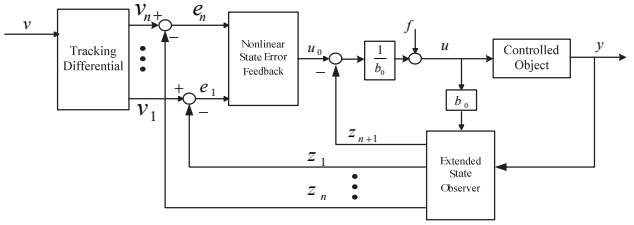


Fig. 4. Control diagram of ADRC.

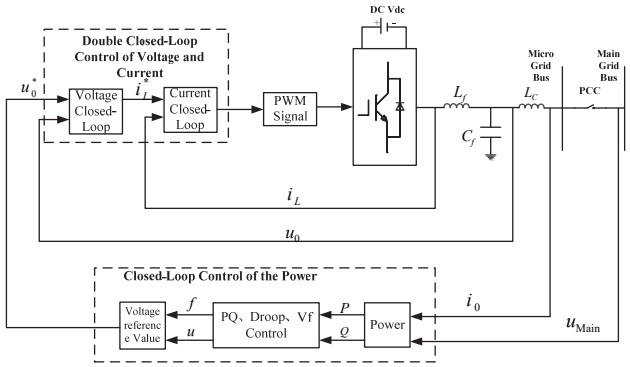


Fig. 5. Control diagram of an interface inverter in a microgrid.

A control diagram of an interface converter in a microgrid is mainly composed of three closed loops, as shown in Fig. 5.

The outer most loop is used to control the power. By measuring the main grid voltage $u_{main}$ and current $i_0$, the active and reactive power can be calculated. Meanwhile, based on the operation mode of each DG, by using the PQ, droop or Vf control, the reference voltage of the inner control loop can be derived. The inner control diagram consists of voltage and current loops. The output of the voltage closed-loop is the reference value of the current closed loop. The current reference is calculated by using the voltage reference and the measured voltage. Meanwhile, PWM signals are generated by the inner current loop in order to drive the IGBTs and to realize the desired microgrid operation. This double loop system, including both voltage and current closed-loops, can rapidly track the power references, which makes the inverter behave as a voltage source. The dynamics and control accuracy can be further enhanced by using an inner current loop [24], [25].

In order to increase the dynamic response of the inner current loop and further enhance the control accuracy, the error should be eliminated with the designed controller. In the meantime, the impact of parameter deviations should also be considered. Hence, the second-order ADRC controller is employed to better track system dynamics. By focusing on the current in the d-q axis, the second-order ADRC controller is designed.

Based on the control algorithm of the ADRC, $u_d$ is selected as the control variable in the d axis to fast track the reference current $i_{dref}$. A control diagram based on ADRC for $i_d$ is shown in Fig. 6.

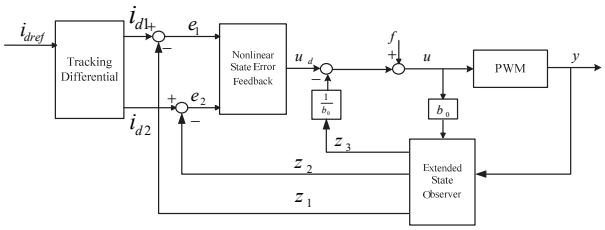


Fig. 6. Control diagram of an ADRC-based current control for $i_d$.

Here, the coupling term is regarded as a disturbance. By using ESO, the disturbance can be estimated. At the same time, by using ADRC, the disturbance can be compensated. Therefore, the decoupling control can be achieved.

It is set that $\omega_d^{'} = u_d + \omega L_f i_{Lq}$ and $\omega_q^{'} = u_q + \omega L_f i_{Ld}$. Substituting the above expressions into (7) yields:

$$\begin{cases} L_f \dfrac{di_{Ld}}{dt} = \omega_d^{'} - u_{od} - r i_{Ld} \\ L_f \dfrac{di_{Lq}}{dt} = \omega_q^{'} - u_{oq} - r i_{Lq} \end{cases} \tag{8}$$

Since $\omega_d^{'}$ and $\omega_q^{'}$ can be considered as an internal disturbance and the changes of $i_d$ and $i_q$ are only related to the physical model, the coupling of $i_d$ and $i_q$ can be realized.

Taking the design of a second-order control diagram as an example, the third-order ESO is the critical part in designing the ADRC controller. The most important part of the ADRC is to estimate disturbances in real-time. Based on this real-time result, compensation can be achieved. The ESO can effectively estimate the overall disturbance in a system, including external disturbances, e.g., noises, and internal disturbances, e.g., parameter derivations. Hence, the original system can be improved. Based on the design principle of the n-order ESO in the ADRC theory, the estimator of $i_d$ is established as follows:

$$\begin{cases} e_1 = z_1 - i_d \\ \dot{z}_1 = z_2 - \beta_{01} e_1 \\ \dot{z}_2 = z_3 - \beta_{02} fal(e_1) + b_0 u \\ \dot{z}_3 = -\beta_{03} fal(e_1) \end{cases} \tag{9}$$

where $z_1$, $z_2$ and $z_3$ are the states under estimation, $z_1$ follows $i_d$, $z_2$ follows $i_q$, $z_3$ follows the total disturbance of the system including internal disturbances, coupling terms, external disturbances, etc., $b$ is the estimated value of $b$, and fal($e_1$) is a nonlinear function with the same sign as $e_1$.

By discretizing (9), it is achieved that:

$$\begin{cases} e_1(k) = z_1(k) - i_d(k) \\ z_1(k+1) = z_1(k) + T * \left( z_2(k) - \beta_{01} e_1(k) \right) \\ z_2(k+1) = z_2(k) + T * \left( z_3(k) - \beta_{02} fal(e_1(k)) \right) + b_0 u(k) \\ z_3(k+1) = z_3(k) - T * \beta_{02} fal(e_1(k)) \end{cases} \tag{10}$$

where $T$ is the sampling period.

The design of TD is shown as follows. In the PID control, there is always a trade-off between a fast response and

over-shoot. In order to solve this problem, a predefined transient period is commonly used to extract the error signal, and the step reference can be smoothed and changed to a ramped signal. Hence, the over-shoot can be weakened. However, in ADRC, the error signal can be accurately extracted by using a TD unit. Therefore, a fast response can be realized without over-shoot. Meanwhile, the differential signal of the system response can also be achieved. Therefore, the range of the system parameters can be improved.

Here the complex function of the speed optimum control $u=fhan(x_1, x_2, r, h)$ is adopted. With the sampling period $T$, the discretized TD can be expressed as:

$$\begin{cases} fh = fhan((x_1(k)-v(k)), x_2(k), r_0, h_0) \\ x_1(k+1) = x_1(k) + T * x_2(k) \\ x_2(k+1) = x_2(k) + T * fh \end{cases} \tag{11}$$

The variable $x_1(k)$ is replaced by $x_1(k)$ - $v(k)$ in order to realize the fast tracking of $v(k)$. The variable $h$ is replaced by $h_0$, and $h_0$ should be independent and larger than $h$ so that the noise amplification of the differential term can be effectively eliminated. The variable $h_0$ is called the filter factor of TD, and $r_0$ is used to determine the rate of the transient period.

The design of the NSEF is shown below. Based on the speed optimum feedback function with damping, the nonlinear error feedback control can be designed and discretized as follows:

$$\begin{cases} u_0(k) = -fhan(e_1(k), ce_2(k), r, h_1 \\ u(k) = u_0(k) - \dfrac{z_3(k)}{b_0} \end{cases} \tag{12}$$

By combing (10), (11) and (12), a critical ADRC controller for the d axis is derived. By using the same method, an ADRC controller for the q axis can be also obtained. Hence, the control of the output voltage in the q axis can be realized. In Fig.5, after getting $v_d$ and $v_q$, the modulation wave for PWM generation can be derived by calculating $M$ and $\theta$. Finally, the drive signals for IGBTs can be achieved.

### C. Design of the Controller Parameters

The values of the parameters in the ESO, TD and NSEF in an ADRC-based microgrid controller significantly impact the performance of the control diagram. Based on the separation principle, the parameters of each control unit can be individually designed. The parameters to be designed in each of the units are h, $r_0$ and $h_0$ in TD, $\beta_{01}$, $\beta_{02}$, $\beta_{03}$ and $b_0$ in ESO and $c$ and $r$ in NSEF.

For the TD control unit, the procedure of the parameter design is shown below. The simulation step $h$ should be selected to be as small as possible. Meanwhile, it should ensure a sufficient stability margin and it should meet the requirement of computational capability. Hence, the parameter deviation in the system can be simulated. In the example system, $h$ is selected as 5e-5.

The variable $r_0$ is used to determine the rate of the transient process. A larger $r_0$ can lead to a faster transient process. However, the value of $r_0$ is limited to the system capability. Normally, $r_0$ is selected as [27]:

$$r_0 = \frac{0.0001}{h^2} \tag{13}$$

By considering the limitations of the system, $r_0$ is set to 45000 here.

The variable $h_0$ should be larger than $h$ so that large oscillations can be eliminated. In the practical simulation cases, $h_0$ is set to 5e-3.

For the ESO unit, the design procedure is shown below. The selection of $\beta_{01}$, $\beta_{02}$ and $\beta_{03}$ has a tight relationship with the simulation step. After determining the simulation step, the value of $\beta_{01}$, $\beta_{02}$ and $\beta_{03}$ can be confirmed by using the following formula:

$$\beta_{01} = \frac{1}{h} \tag{14}$$

$$\beta_{02} = \frac{1}{1.6h^{1.5}} \tag{15}$$

$$\beta_{03} = \frac{1}{8.6h^{2.2}} \tag{16}$$

In a practical system, $\beta_{01}$=2000, $\beta_{02}$=55902, $\beta_{01}$=2127000, and $b_0 = 5$.

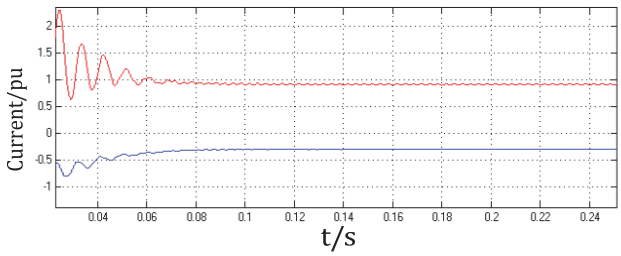


Fig. 7. Waveforms of $i_d$ and $i_q$.

### D. Stability Verification of ADRC

The estimation of system disturbance based on ESO is the most critical part of the design procedure of the ADRC. Therefore, the design of the ESO plays the most important role in the ADRC. The stability of the ESO significantly impacts the stable operation of the ADRC. In this paper, the Lyapunov approach is used to determine the stability of the ESO.

Based on the aforementioned analysis, there are coupled terms between $i_d$ and $i_q$. These coupled terms are regarded as a disturbance in the ADRC design so that the decoupled control of $i_d$ and $i_q$ can be achieved. Take the ADRC design for $i_d$ as an example. By analyzing the results in Fig.3, $i_q$ exists in the control loop of $i_d$, while the impact of $i_q$ on $i_d$ is insignificant, as shown in Fig. 7,

where the red line represents $i_d$ and the blue line represents $i_q$. Since this impact is very small, it can be regarded as a constant, namely $\omega_n$. For a third-order nonlinear system, it

can be simplified as a second-order nonlinear system to conduct the stability analysis.

The second-order nonlinear system in the d axis can be shown as:

$$\begin{cases} \dot{x}_1 = x_2 \\ \dot{x}_2 = x_3 + bu \\ \dot{x}_3 = 0 \\ y = x_1 = i_d \end{cases} \tag{17}$$

Since the variable $x_3$ is equal to $\omega_n$ and is kept constant, it can be derived that $\dot{x}_3 = 0$. The ESO of the system can be established as:

$$\begin{cases} e_1 = z_1 - i_d \\ \dot{z}_1 = z_2 - \beta_{01} e_1 \\ \dot{z}_2 = z_3 - \beta_{02} fal(e_1) + bu \\ \dot{z}_3 = 0 \end{cases} \tag{18}$$

where $\beta_{01}$ and $\beta_{02}$ are real numbers that are larger than zero. (1) is the determined nonlinear function.

Subtracting (18) from (17) yields:

$$\begin{cases} e_1 = z_1 - i_d, e_2 = z_2 - x_2 \\ \dot{e}_1 = e_2 - \beta_{01} e_1 \\ \dot{e}_2 = -\beta_{02} fal(e_1) \end{cases} \tag{19}$$

By using the Lyapunov theory, for validating the stability of (19), a constant function $V(x)$ should be established. This fulfills the requirements of (1) $V(0) = 0$; (2) $V(0) > 0$ for an arbitrary $x \neq 0$; and (3) $V(x)$ has a first-order differential and the differential of $V(x)$ is smaller than 0. When satisfying all of the above requirements, $V(x)$ is asymptotically stable.

The function $V(x)$ is created as:

$$V(e_1, e_2) = \frac{1}{2} {e_2}^2 + \int_0^{e_1} \beta_{02} fal(e) de$$

It can be derived from (11) that:

$$fal(e, \alpha, \delta) = \begin{cases} |e|^{\alpha} sign(e) \cdots\cdots\cdots |e| > \delta \\ e / \delta^{1-\alpha} \cdots\cdots\cdots\cdots\cdots |e| \le \delta \end{cases}$$

Here the function of $V(e_1, e_2)$ is established for *fal*(e) with the constraints $|e| > \delta$ and $|e| \le \delta$. Thereby, the stability is demonstrated. Here, $\alpha = 1/2$.

When $|e| > \delta$, $V(e_1, e_2)$ is shown as:

$$V(e_1, e_2) = \frac{1}{2} {e_2}^2 + \int_0^{e_1} \beta_{02} |e|^{\alpha} sign(e) de \tag{20}$$

where $\frac{1}{2} e_2^2 > 0 (e_2 \neq 0)$.

Assuming that $V_1 = \int_0^{e_1} \beta_{02} |e|^{\alpha} sign(e) de$, it is obtained that:

- When $e_1 > 0$,

$$V_1 = \int_0^{e_1} \beta_{02} |e|^{\alpha} sign(e) de = \beta_{02} \frac{2}{3} |e_1|^{\frac{3}{2}} > 0$$

- When $e_1 < 0$,

$$V_2 = -\int_0^{e_1} \beta_{02} |e|^{\frac{1}{2}} de = \int_{e_1}^{0} \beta_{02} |e|^{\frac{1}{2}} de = \beta_{02} \frac{2}{3} |e_1|^{\frac{3}{2}} > 0$$

Hence, for any $V(e_1, e_2)$ ($e_1 \neq 0$, $e_2 \neq 0$), it can be concluded that $V(e_1, e_2) > 0$.

Furthermore, since

$$\frac{\partial V}{\partial e_1} = \beta_{02} |e_1|^{\frac{1}{2}} sign(e_1), \frac{\partial V}{\partial e_2} = e_2$$

It is achieved that:

$$\begin{aligned} \dot{V} &= \frac{\partial V}{\partial e_1} \dot{e}_1 + \frac{\partial V}{\partial e_2} \dot{e}_2 \\ &= \beta_{02} |e_1|^{\frac{1}{2}} sign(e_1)(e_2 - \beta_{01} e_1) + e_2 (-\beta_{02} |e_1|^{\frac{1}{2}} sign(e_1)) \\ &= -\beta_{01} \beta_{02} |e_1|^{\frac{1}{2}} e_1 sign(e_1) \\ &= -\beta_{01} \beta_{02} |e_1|^{\frac{1}{2}} |e_1| < 0 \end{aligned}$$

Hence, $\dot{V}$ is negative definite and (19) is asymptotically stable.

When $|e| \le \delta$, $V(e_1, e_2)$ is shown as:

$$V(e_1, e_2) = \frac{1}{2} {e_2}^2 + \int_0^{e_1} \beta_{02} e / \delta^{1-\alpha} de \tag{21}$$

It can be easily seen that $V(e_1, e_2) > 0$ and it is positive definite.

Further, it is reached that:

$$\frac{\partial V}{\partial e_1} = \beta_{02} e / \delta^{1-\alpha}, \frac{\partial V}{\partial e_2} = e_2$$

where:

$$\begin{aligned} \dot{V} &= \frac{\partial V}{\partial e_1} \dot{e}_1 + \frac{\partial V}{\partial e_2} \dot{e}_2 = \beta_{02} e / \delta^{1-\alpha} (e_2 - \beta_{01} e_1) + e_2 (-\beta_{02} e / \delta^{1-\alpha}) \\ &= -\beta_{01} \beta_{02} e_1^2 / \delta^{1-\alpha} < 0 \end{aligned}$$

Hence, $\dot{V}$ is negative definite and (20) is asymptotically stable.

Taken altogether, for the conditions of $|e| > \delta$ and $|e| \le \delta$, although the function *fal*(e) is not exactly the same, the corresponding ESO systems are asymptotically stable based on the Lyapunov stability criteria.

## IV. Simulation Validations

In order to verify effectiveness of the ADRC on microgrid mode transitions and load variations, a simulation platform including two DGs is implemented as shown in fig. 8.

In this platform, droop control is used for DG #1 to support the voltage and frequency of the microgrid, and PQ control is used for DG #2 to provide constant active and reactive power support. The system parameters are shown below. The AC side voltage is 400 V, and the voltage rating of the main grid is 10 kV. The total load of the system is 14 kW. DG #1 and #2 are adjustable to provide the required active and reactive powers. The main parameters about the Microgrid are shown in Table 1.

Because PQ control is used for DG #2, its output power should be constant, as shown in Fig. 9-a, Fig. 9-b and Fig.

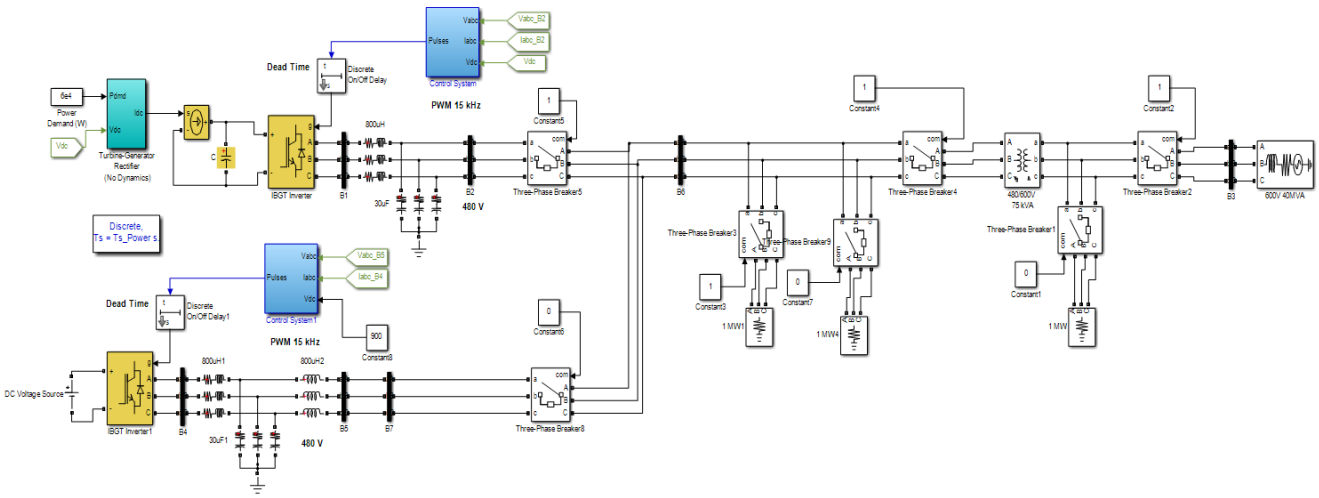


Fig. 8. The simulation structure diagram.

TABLE I
MAIN PARAMETERS OF THE MICROGRID

| OBJECT | PARAMETRE |
|---|---|
| DG1 | DC voltage:Vdc=700V<br>Switch frequency：5KHz<br>Filter parameters：$L_f$=1.6mH, $C_f$=40uF<br>Attachment inductance：$L_c$=1mH<br>Droop control settings: $P_0$=14KW, $Q_0$=0KVar, $V_0$=311V, $f_0$=50Hz |
| DG2 | DC voltage:$V_{dc}$=700V<br>Switch frequency：5KHz<br>Filter parameters：$L_1$=1.2mH, C=20uF, $L_2$=0.8mH<br>Power factor：Q=1 |
| Rated Voltage and Frequency | 380V/50Hz |
| LOAD 1 | P=9 kW，Q=0kVar |
| LOAD 2 | P=5 kW，Q=0kVar |

9-c.

Since there are no significant dynamics involved in these waveforms, DG#1 is selected as the main research objective for further study.

### *A. Islanding Operation*

When a system runs in the islanding mode, the microgrid and the main grid are totally separated. The frequency and voltage of the microgrid are supported by the DGs. In this case, the frequency and voltage are generated by DG #1 with the droop control, while the constant active and reactive powers are generated by DG #2. In the simulation results, the red lines represent the curves derived from the PID control, and the blue lines represent the curves derived from the ADRC.

The results for a smooth starting up process are shown below. Before t = 0.3 s, the starting up procedure gradually

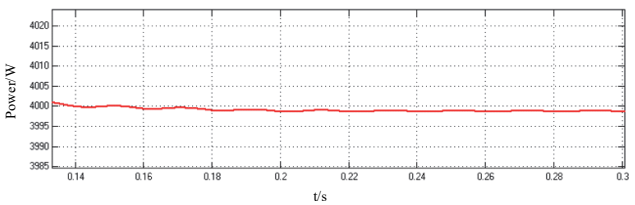


(a) Starting up procedure.

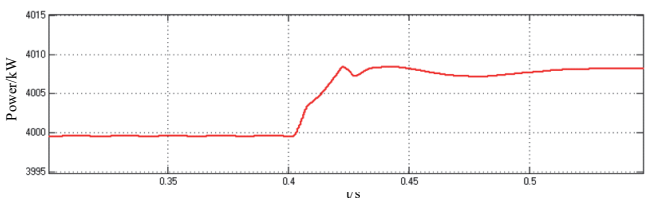


(b) Load variation (decreasing) procedure at t = 0.4 s.

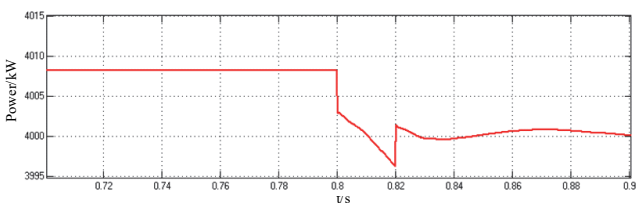


(c) Load variation (increasing) procedure at t = 0.8.

Fig. 9. The Output Power of DG #2.

changes to the steady state. The local active load is 14 kW and the local reactive power is 0 kVar. The active and reactive powers delivered by DG #1 are 10 kW and 0 kVar, respectively, and those delivered by DG #2 are 4 kW and 0 kVar. The output voltage, current, frequency and power of DG #1 are shown in Fig. 10.

It can be seen from Fig. 10 that during the starting up procedure, the voltage and current inside a microgrid are slightly distorted at the beginning, while they come to the normal state after a short period of time. From this standing point, there are no obvious differences. The output waveforms are composed of three parts. Among them, the red

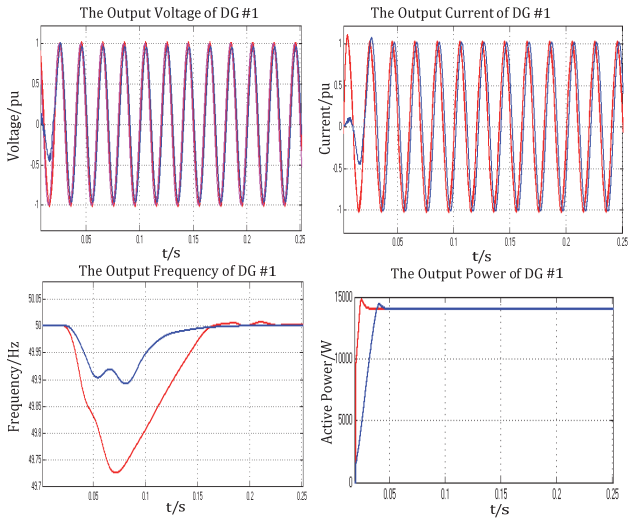


Fig. 10. Results of the microgrid starting up procedure for islanding operation (t = 0 ~ 0.3 s).

one is the result with the PID control. The blue one is the result with the ADRC control. The pink one is the voltage of the main grid. During the starting period, these three curves are almost equal. However, it can be clearly seen from the frequency curve that the ADRC has better performance when compared to the PID control. This shows that during the starting period, the ADRC is more effective with larger disturbances.

At t = 0.4 s, the load in the microgrid is suddenly reduced. In particular, the active power load is reduced by 9 kW. Since DG #2 works in the PQ control mode, its output power does not change. Hence, the system response regarding this load disturbance can be also overcome by DG #1 with droop control. When the load decreases, the output voltage of DG #1 does not change, and the output current decreases. Hence, the output power decreases to compensate the impact of load variations. In Fig. 11, when the load is suddenly changed, the ADRC has better performance in terms of either steady-state errors or transient adjusting time when compared to the conventional PID control.

At t = 0.8 s, the load inside the microgrid increases. In particular, the active power load increases to 9 kW. It can be seen from Fig. 12 that with the recovery of the load, the microgrid voltage, current and frequency gradually recover as well. However, since there is still an error in the PID-controlled system when decreasing the load, system oscillations can be found in the PID-controlled system. This impact can be clearly seen from the voltage and current waveforms. For this standing point, the ADRC still has better performance when compared to the PID control.

Meanwhile, it can be seen from Fig. 11 and 12 that the ADRC can rapidly estimate the disturbance when it appears, and that it can eliminate the impact of the disturbance and ensure a smooth transient process.

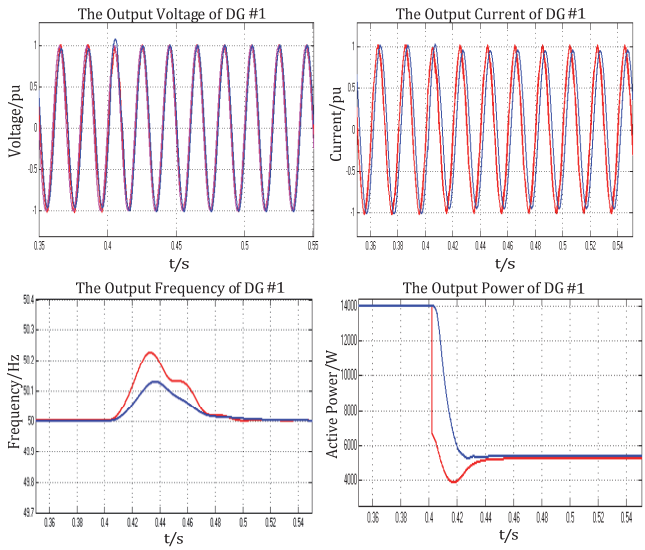


Fig. 11. Waveforms of the microgrid load variation (decreasing) procedure at t = 0.4 s.

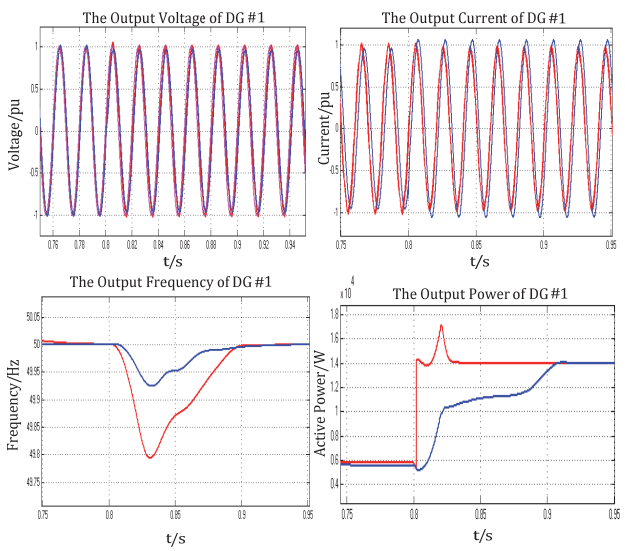


Fig. 12. Waveforms of the microgrid load variation (increasing) procedure at t = 0.8.

## B. *Grid-Connected Operation*

In grid-connected operation, the microgrid frequency and voltage are supported by the main grid. The DGs mainly impact the performance in terms of load variation and they guarantee the stable operation of the system.

At t = 0 ~ 0.3 s, the microgrid is started and kept in the grid-connected mode. During this period of time, the microgrid turns into the steady state. The local active load is 14 kW and the reactive load is 0 kVar. The output active power of DG #1 is 10 kW and the output reactive power is 0 kVar. Meanwhile, the output active power of DG #1 is 4 kW and the output reactive power is 0 kVar. The output voltage, current, frequency and power are shown in Fig. 13.

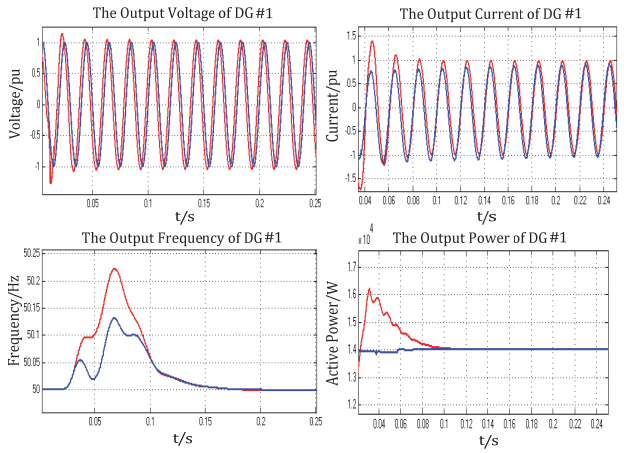


Fig. 13. Waveforms of the microgrid starting up procedure for grid-connected operation (t = 0 ~ 0.3 s).

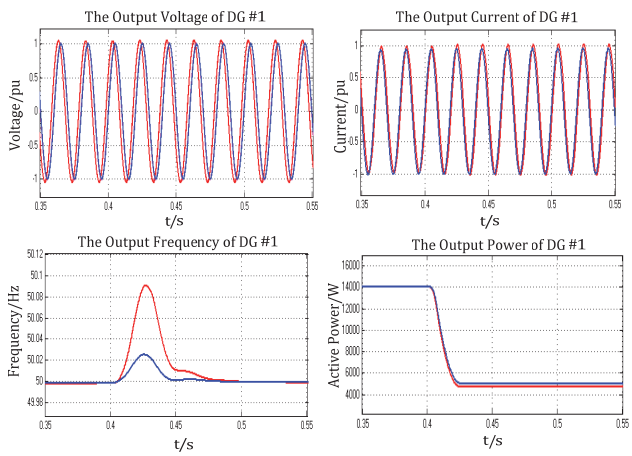


Fig. 14. Waveforms of the microgrid load variation (decreasing) procedure at t = 0.4 s.

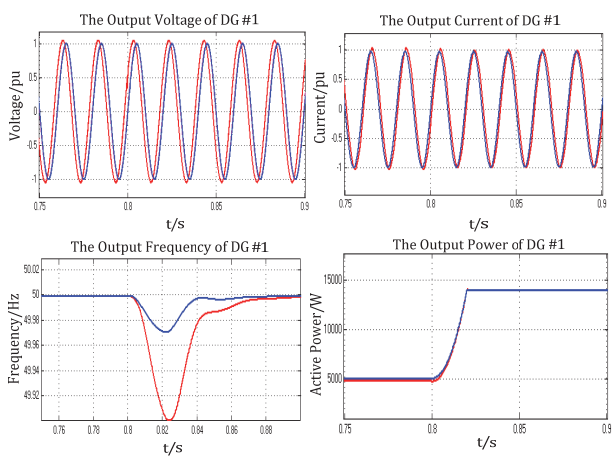


Fig. 15. Waveforms of the microgrid load variation (increasing) procedure at t = 0.8.

At t = 0.4 s, the local active load decreases by 9 kW while the reactive load does not change. The output voltage, current, frequency and power are shown in Fig. 14.

At t = 0.8 s, the local load increases by 9 kW while the reactive power is kept the same. The output voltage, current, frequency and power are shown in Fig. 15.

It can be seen from Fig. 13 that the output waveforms for the ADRC and PID control are both acceptable during the starting up period. With the ADRC control, the output voltage is almost the same as the main grid voltage. However, with the PID control, although the voltage amplitudes are almost in accordance with each other, there are still phase differences. In the current waveforms, besides the phase error, there are obvious current over-shoots. For frequency variations, the adjusting time for each control method is almost the same, while the maximum frequency under the ADRC is only 50.14 Hz. The maximum frequency under the PID control is about 50.22 Hz, which is higher than that for the ADRC. It can be further concluded that with a sudden disturbance, the ADRC can estimate the disturbance and compensate it to keep the oscillations of the system within a small range. Hence, the system stability can be guaranteed.

At t = 0.4 s, the local active load suddenly increased to 9 kW. It can be seen from the voltage waveform that with the load variation, the voltage curve in Fig. 14 becomes distorted. However, since the voltage is supported by the main grid, its amplitude is not changed. However, with the PID control, a phase differences appear. Hence, the performance of the ADRC is better than the PID control from this aspect.

A similar phenomenon can be also seen from the current waveform. For the frequency waveform, it can be seen that the frequency variation with the PID control is much higher than the ADRC. This further demonstrate that the ADRC has better performance when compared to the PID control in terms of anti-disturbance capability.

In Fig. 15, the advantages of the ADRC can be further verified. When the system is under a disturbance, the ADRC uses its own capability of anti-disturbance, and the variations induced by the disturbance can be effectively eliminated. Hence, after the disturbance, the system can get back to the normal state smoothly.

### *C. Operation Mode Transition*

The operation mode transitions of a microgrid mainly include “grid-connected to islanding” and “islanding to grid-connected”. These two mode transition procedures are key factors to identify if a microgrid is feasible or not. Here the ADRC and conventional PID controllers are still used for comparison.

The results for the mode transition from the grid-connected mode to the islanding mode are shown and discussed below.

The microgrid is started in the grid-connected mode. At t = 0.4 s, an intentional islanding occurs which drives the microgrid from the grid-connected mode to the islanding mode. The critical loads are supplied by the DGs inside the microgrid.

At t = 0.4 s, since intentional islanding occurs, the switch at the PCC turns off, and the frequency and voltage inside the microgrid are supported and stabilized by the DGs. Since DG #1 runs in the droop-controlled mode, the frequency and voltage support is provided by DG #1. It can be seen from Fig. 16 that at the moment of disconnection of the microgrid at the PCC, large voltage and current over-shoots are clearly shown with the PID control. However, with the ADRC method, variations of the voltage and current are reduced to a large extend. It can also be clearly seen from the frequency waveforms that the ADRC is better than the PID control in terms of oscillation, transient response rate and steady-state error. The ADRC features fast detection and elimination of the disturbance and it demonstrates its outstanding capability to improve the performance under extremum conditions. Meanwhile, as long as the source power inside the microgrid is enough to feed the load in the microgrid, the variations of the frequency and voltage are small enough to ensure a smooth mode transition.

At t = 1.4 s, the main grid is ready for the connection of a microgrid. Meanwhile, the microgrid adjusts its voltage and frequency to keep them the same as those of the main grid. Then the switch at the PCC is closed to conduct the mode transition.

During islanding operation, the internal voltage and frequency are supported by the DGs. In the simulation, they are provided by DG #1 with droop control. However, since droop control is realized based on voltage and frequency deviations, during the islanding operation, they can have differences from those of the main grid. If directly connecting a microgrid to the main grid, there can be significant oscillations that may damage the equipment. Hence, before turning to the grid-connected mode, the microgrid frequency and amplitude should be controlled to values similar to those of the main grid. In Fig. 17, it can be seen that at the moment of grid-connection, sudden changes can be found in the voltage and current waveforms. The over-shoot induced in the PID control is much higher than that in the ADRC. Similar results can be found in the waveforms of the frequency.

By comparing the simulation results, it can be found that the ADRC has better performance in terms of disturbances. It can rapidly compensate the disturbance and ensure stable system operation. Its control performance is better than the conventional PID control. Meanwhile, when implementing droop and PQ control, the ADRC still gives better results. Coordinated control among multiple DGs can be achieved.

In microgrids, due to different load characteristics, the system operation may be changed. Resistive loads and inductive-resistive loads can result in different dynamic features during microgrid mode transitions. For example,

when the microgrid operation changes from the grid-connected mode to the islanded mode at $t = 0.4$ s or

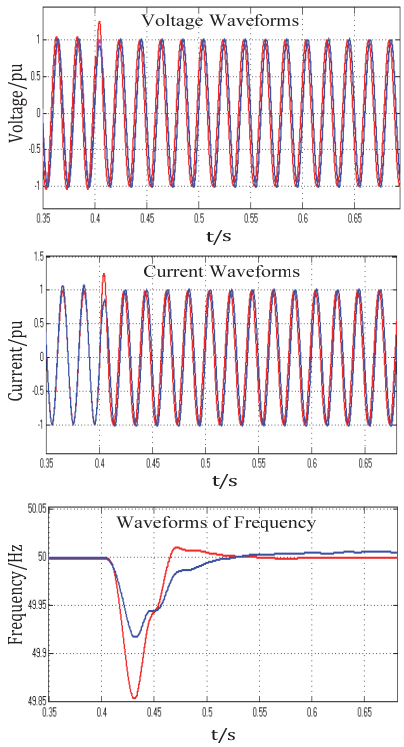


Fig. 16. Waveforms for the mode transition from the grid-connected mode to the islanding mode.

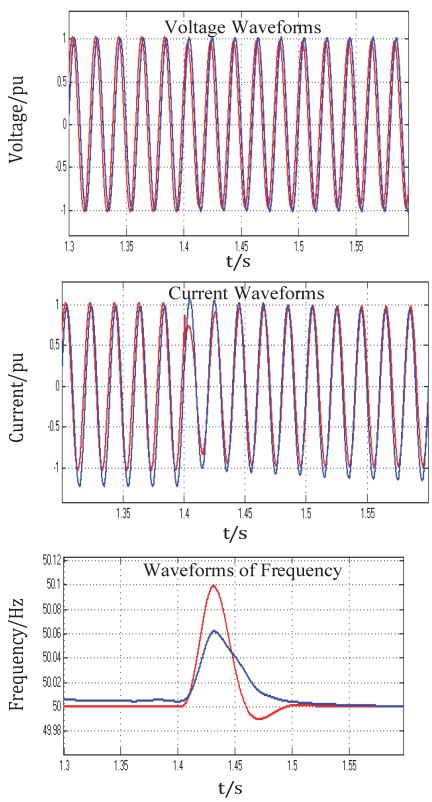


Fig. 17. Waveforms for the mode transition from the islanding mode to the grid-connected mode.

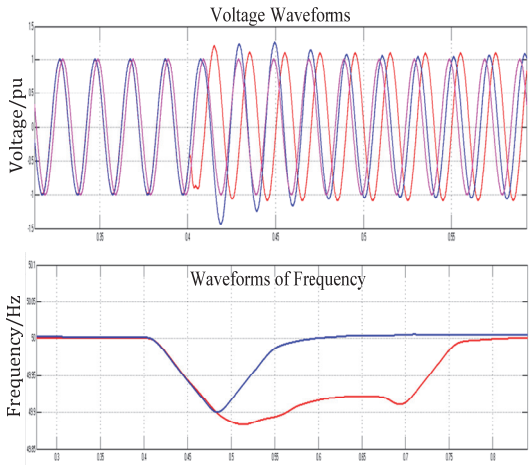


Fig. 18. Waveforms for the mode transition from the islanding mode to the grid-connected mode by using inductive-resistive loads.

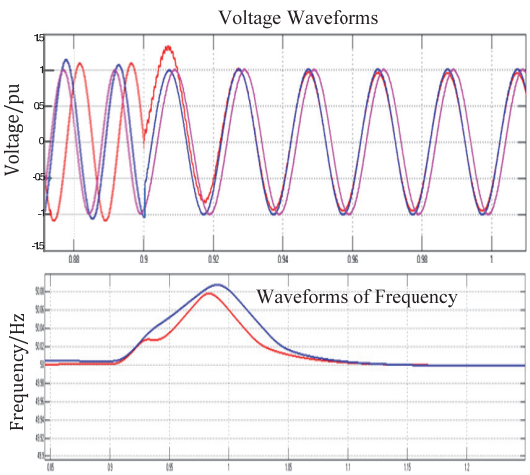


Fig. 19. Waveforms for the mode transition from the grid-connected mode to the islanding mode by using inductive-resistive loads.

when the microgrid operation changes from the islanded mode to the grid-connected mode at $t$ = 0.9 s, simulation tests using inductive-resistive loads are conducted. In the simulations, the local load is set to 14 kW and 5 kVar. The voltage curves and output power curves are shown in Fig. 18 and Fig. 19, respectively, where the red curves show the results using the PID control and the blue curves shows the results using the ADRC control algorithm. Meanwhile, the magenta curve shows the grid voltage.

It can be seen that although the change of loads has some impact on the control performance, the voltage and frequency can be stabilized in a very short time. The oscillations are all controlled within an acceptable range. Meanwhile, the control performance of the ADRC control algorithm is still better than that of the PID control.

*D. Operation Situation under Harmonics*

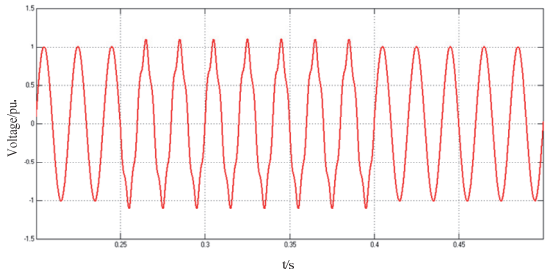


Fig. 20. Waveforms for the harmonic voltage.

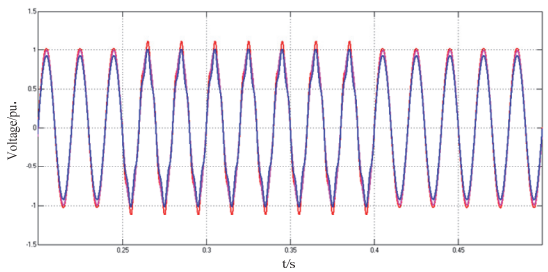


Fig. 21. Waveforms for the voltage change under harmonics.

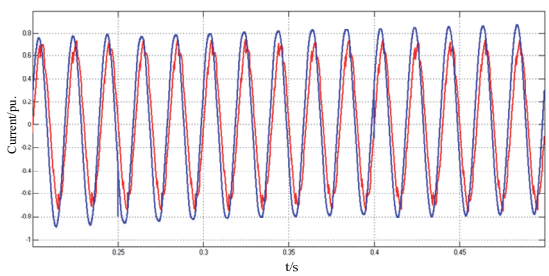


Fig. 22. Waveforms for the current change under harmonics.

In order to verify the control capability for disturbances of the ADRC, a nonlinear harmonic disturbance was imitated in the simulation process, by setting up the harmonic generation time, amplitude, frequency, phase, etc. of the programmable three-phase source. The specific process is as follows:

At t=0.25 seconds, the harmonic disturbance was added where the harmonic amplitude is equal to 1.08 times the unit amplitude (in per unit) and the phase is -450. The waveforms of the harmonic voltage are shown in Fig.20.

At t=0.4 seconds, the harmonic effect is finished, and the system returns to the normal operation process which was shown in Fig. 20.

The curves of the voltage and current under harmonics are shown in Fig.21 and Fig.22, respectively.

In the simulation results, the pink lines represent the reference voltage and current curve, the red lines represent the voltage and current curve under the control of the PID, and the blue lines represent the voltage and current curve under the control of the ADRC.

It can be seen that the PID and ADRC have better operation results before adding a harmonic disturbance. When the harmonic distortion was added as t=0.25 seconds,

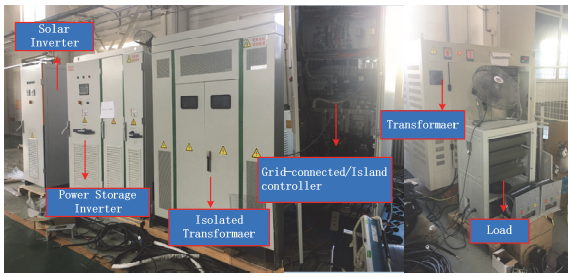


Fig. 23. Experimental testing system.

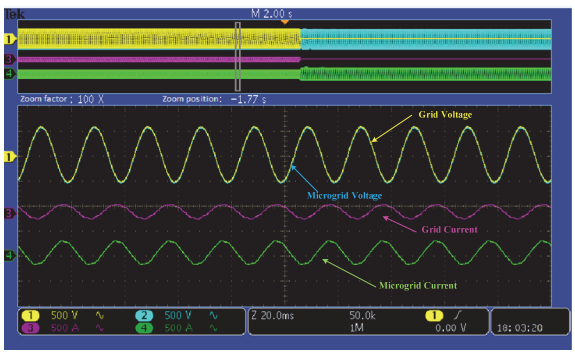


Fig. 24. Experimental waveforms in the grid-connected mode.

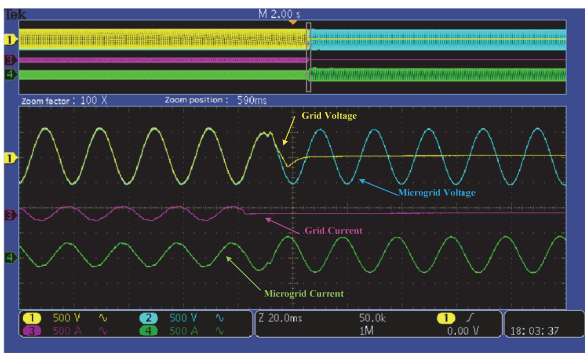


Fig. 25. Experimental waveforms of a transition from the grid-connected mode to the islanding mode.

all of the voltage curves have some deformation. However, the amplitude and phase of the voltage curve are almost identical to the grid voltage under the control of the ADRC. In addition, the amplitude of the voltage curve under the control of the PID is obviously changed. In the current curve, it is still obvious that the control effect of the ADRC is better than that of the PID after adding the harmonic disturbance, and that the current curve under the PID control is not smooth.

After t=0.4 seconds, the harmonic disturbance disappears and the system returns to normal operation.

The simulation results show that because the ADRC itself has the characteristics of disturbance identification and correction, the control capability of the ADRC in the face of unknown interference is much stronger than that of the PID.

## V. Experiment Validations

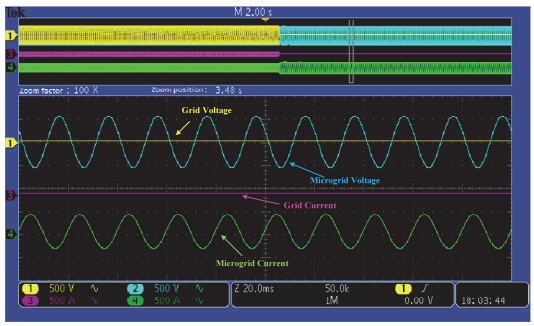


Fig. 26. Experimental waveforms in the islanding mode.

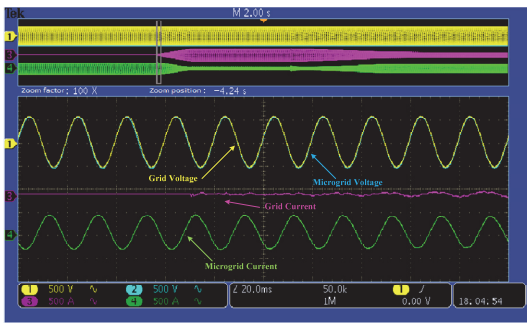


Fig. 27. Experimental waveforms for a transition from the islanding mode to the grid-connected mode.

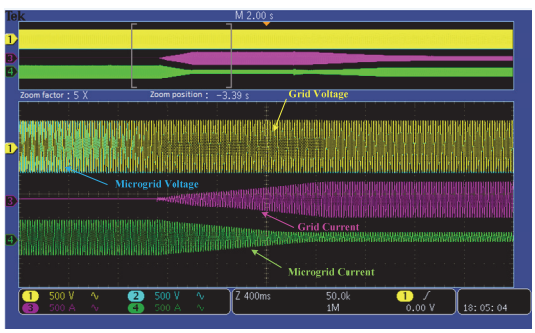


Fig. 28. Experimental waveforms of the power exchange in a transition from the islanding mode to the grid-connected mode.

To demonstrate the feasibility of the ADRC controller, an experimental platform was built, as shown in Fig. 23. Meanwhile, the experimental results are shown in Fig. 24 - Fig. 28.

In these experimental results, the yellow lines represent the grid voltage, the purple lines represent the grid current, the blue lines represent the microgrid voltage, and the green lines represent the microgrid current. From the experimental results, it can be seen that the system can run in a stable state whether in a transition from the grid-connected mode to the islanding mode or in a transition from the islanding mode to the grid-connected mode by using the ADRC.

## VI. Conclusions

In order to realize smooth mode transitions and the stabilization of a microgrid, an advanced ADRC is proposed

and applied to microgrid controller design in this paper. A second-order ADRC for microgrid operation is implemented. This controller can ensure transitions between the grid-connected mode and the islanding mode. Meanwhile, it works for the cases of load variations. By using a third-order ESO, the ADRC can effectively detect and eliminate the internal and external disturbances. As a result, it can achieve flexible interactions between a microgrid and the main grid. In the simulation and experiment results, it can be seen that the ADRC has better performance than the conventional PID control. Meanwhile, the stability of the third-order ESO in the ADRC is also verified by using Lyapunov criteria. Hence, smooth microgrid mode transitions can be guaranteed.

## ACKNOWLEDGMENT

Supported by "the Fundamental Research Funds for the Central Universities" (Project Number: 2572017BB13).

## REFERENCES

[1] European Commission, "Towards smart power networks lessons learned from European research FP5 projects," *Luxembourg: Office for Official Publications of the European Communities*, 2005.

[2] R. Lasseter and P. Piagi, "Providing premium power through distributed resources," in *Proceedings of the 33rd Annual Hawaii International Conference on System Science*, pp. 1-9, Jan. 2000.

[3] N. Hatziargyriou, H. Asano, and R. Iravani, "Microgrids: an overview of ongoing research, development, and demonstration projects," *IEEE Power Energy Mag.*, Vol. 5, No.4, pp. 78-94, Apr. 2007.

[4] S. Krishnamurthy, T. M. Jahns, and R. H. Lasseter, "The operation of diesel gensets in a CERTS microgrid," in *IEEE Power and Energy Society General Meeting: Conversion and Delivery of Electrical Energy in the 21st Centrury*, pp. 9, Jul. 2008.

[5] I. S. Bae and J. O. Kim, "Reliability evaluation of customers in a micro grid," *IEEE Trans. Power Syst.*, Vol. 23, No. 3, pp. 1416-1422, Mar. 2008.

[6] S. Kwon, J. Kim, I. Song, and Y. Park, "Current development and future plan for smart distribution grid in Korea," in *Proceedings of the IET-CIRED Seminar 2008: SmartGrids for Distribution*, pp. 4, Jun. 2008.

[7] N. Pogaku, M. Prodanovic, and T. C. Green, "Modeling, analysis and testing of autonomous operation of an inverter-based microgrid," *IEEE Trans. Power Electron.*, Vol. 22, No. 2, pp. 613-625, Mar. 2007.

[8] S. Morozumi, "Micro-grid demonstration projects in Japan," in *Proceedings of the 4th Power Conversion Conference*, pp. 635-642, Apr. 2007.

[9] X. Lu, J. M. Guerrero, K. Sun, and J. C. Vasquez, "An improved droop control method for DC microgrids based on low bandwidth communication with DC bus voltage restoration and enhanced current sharing accuracy," *IEEE Trans. Power Electron.*, Vol. 29, No. 4, pp. 1800-1812, Apr. 2014.

[10] F. Blaabjerg, Z. Chen, and S. B. Kjaer, "Power electronics as efficient interface in dispersed power generation systems," *IEEE Trans. Power Electron*., Vol. 19, No. 5, pp. 1184-1194, Sep. 2004.

[11] J. M. Carrrasco, L. G. Franquelo, J. T. Bialasiewicz, E. Galvan, R. C. P. Guisado, M. A. M. Prats, J. I. Leon, and N. Moreno-Alfonso, "Power-electronic systems for the grid integration of renewable energy sources:a survey," *IEEE Trans. Ind. Electron*., Vol. 53, No. 4, pp. 1002-1016, Apr. 2006.

[12] C. K. Sao and P. W. Lehn, "Autonomous load sharing of voltage source converters," *IEEE Trans. Power Del.*, Vol. 20, No. 2, pp. 1009-1016, Apr. 2005.

[13] C. T. Lee, C. C. Chu, and P. T. Cheng, "A new droop control method for the autonomous operation of distributed energy resource interface converters," *IEEE Trans. Power Electron.*, Vol. 28, No. 4, pp. 1980-1993, Apr. 2013.

[14] Y. W. Li and C. N. Kao, "An accurate power conrol strategy for power electronics interfaced distributed generation unints operating in a low voltage multibusmicrogrd," *IEEE Trans. Power Electron*., Vol. 24, No. 12, pp. 2977-2988, Dec. 2009.

[15] P. Arboleya, D. Diaz, J. M. Guerrero, P. Garcia, F. Briz, C. Gonzalez-Moran, and J. Gomez Aleixandre, "An improved control scheme based in droop characteristic for microgrid converters," *Electric Power Systems Research*, Vol. 80, No. 10, pp. 1215-1221, Oct. 2010.

[16] J. Qesada, R. Sebastian, M. Castro, and J. A. Sainz, "Control of inverters in a low voltage microgrid with distributed battery energy storage. Part I: Primary control," *Electric Power Systems Research*, Vol. 114, pp. 126-135, Sep. 2014.

[17] M. M. A. Abdelaziz and E. F. El-Saadany, "Maximum loadability consideration in droop-controlled islanded microgrids optimal power flow," *Electric Power Systems Research*, Vol. 106, pp. 168-179, Jan. 2014.

[18] D. Soto, C. Edrington, S. Balathandayuthapani, and S. Ryster, "Voltage balancing of islanded microgrids using a time-domain technique," *Electric Power Systems Research*, Vol. 84, No. 1, pp. 214-223, Mar. 2012.

[19] T. L. Vandoorn, J. V. de Vyver, B. Meersman, B. Zwaenepoel, and L. Vandevelde, "Phase unbalance mitigation by three-phase damping voltage-based droop controllers in microgrids," *Electric Power Systems Research*, Vol. 127, pp. 230-239, Oct. 2015.

[20] F. Shahnia, R. Majumder, A. Ghosh, G. Ledwich, and F. Zare, "Operation and control of a hybrid microgrid containing unbalanced and nonlinear loads," *Electric Power Systems Research*, Vol. 80, No. 8, pp. 954-965, Aug. 2010.

[21] R. Caldon, F. Rossetto, and R. Turri, "Analysis of dynamic performance of dispersed generation connected through inverter to distribution networks," *17th International Conference on Electricity Distribution*, pp. 12-15, May 2003.

[22] S. Barsali, M. Ceraolo, P. Pelacchi, and D. Poli, "Control techniques of dispersed generators to improve the continuity of electricity," in *IEEE Power Engineering Society Winter Meeting*, pp. 789-794, Jan. 2002.

[23] Y. Liu, Q. Zhang, C. Wang, and N. Wang, "A control strategy for microgrid inverters based on adaptive three-order sliding mode and optimized droop controls," *Electric Power Systems Research*, Vol. 117, pp. 192-201,

Dec. 2014.
[24] X. Lu, J. M. Guerrero, K. Sun, and J. C. Vasquez, "An Improved Droop Control Method for DC Microgrids Based on Low Bandwidth Communication With DC Bus Voltage Restoration and Enhanced Current Sharing Accuracy," *IEEE Trans. Power Electron*., Vol. 29, No. 4, pp. 1800-1812, Apr. 2014.
[25] X. Lu, J. M. Guerrero, K. Sun, J. C. Vasquez, R. Teodorescu, and L. Huang, "Hierarchical Control of Parallel AC-DC Converter Interfaces for Hybrid Microgrids," *IEEE Trans. Smart Grid*, Vol. 5, No. 2, pp. 683-692, Mar. 2014.
[26] J. Han, "Control theory-model theory or control theory," *System Science and Math Science*, Vol. 9, No. 4, pp. 328-335, Apr. 1989.
[27] J. Han, "Active Disturbance Rejection Control Technique-the technique for estimating and compensating the uncertainties," *National Defense Industry Press*, 2008.

**Xiaoning Xu** was born in Zibo, China. She received her B.S. and M.S. degrees in Electrical Engineering from the Tianjin University of Technology, Tianjin, China, in 2003 and 2012, respectively. She is presently working towards her Ph.D. degree in the School of Electrical Engineering and Automation, Tianjin University, Harbin, China. In 2007, she joined the Tianjin University of Technology where she is presently working as a Lecturer. Her current research interests include power electronics for renewable energy sources, the analysis of power system, microgrids and energy conversion.

**Xuesong Zhou** was born in Nanchang, China. He received his B.S. degree in Power System and Automation from the South China University of Technology, Guangzhou, China, in 1984; and his M.S. and Ph.D. degrees in Power System and Automation from Tsinghua University, Beijing, China, in 1990 and 1993, respectively. From 1984 to 1987, he was with the Automation Institute of Electric Force, Nanjing, China, where he worked on automatic generation control systems. From 1993 to 2002, he was a Associate Dean in the School of Electrical and Automation Engineering, Qingdao University, Qingdao, China, where he was promoted to Professor. Since 2002, he has been a Distinguished Professor in the School of Automation, Tianjin University of Technology, Tianjin, China, where he served as a doctoral supervisor and as the leader of the key subject of "electrical engineering." His current research interests include power system analysis and control, the application of power electronic technology in power systems, and new energy generation.

**Youjie Ma** was born in Tianjin, China. She received her B.S., M.S. and Ph.D. degrees in Power System and Automation from Tsinghua University, Beijing, China, in 1987, 1990 and 1993, respectively. From 1993 to 2002, she was with the School of Electrical and Automation Engineering, Qingdao University, Qingdao, China, where she was promoted to Professor. Since 2002, she has been a Distinguished Professor in the School of Automation, Tianjin University of Technology, Tianjin, China, where she served as a master's supervisor. Her current research interests include power system analysis and control, and new energy generation.

**Yiqi Liu** received his B.S. degree in Electrical Engineering from the Northeast Agriculture University, Harbin, China, in 2009; and his M.S. degree in Electrical Engineering from the Tianjin University of Technology, Tianjin, China, in 2012. He is presently working towards his Ph.D. degree in the School of Electrical Engineering and Automation, Harbin Institute of Technology, Harbin, China. From 2013 to 2015, he was a Visiting Ph.D. student with the Center for Ultra-Wide-Area Resilient Electric Energy Transmission Networks (CURENT), University of Tennessee, Knoxville, TN, USA, with support from the China Scholarship Council. He joined the Northeast Forestry University, Harbin, China, in 2016, and is presently working as an Associate Professor. His current research interests include power electronics for renewable energy sources, multilevel converters, high-voltage direct-current (HVDC) technology, DC microgrids and energy conversion.